Profile-wide desalinization is associated with increased deep-soil microbial biomass and reduced iron-bound carbon in coastal wetland restoration

Jingwen Gao[1], Pengcheng Jiang[1], Xiaofei Ye[1], Xingna Lin[1], Xuexin Shao[1], Ming Wu[1], Niu Li[1*]

[1] Wetland Ecosystem Research Station of Hangzhou Bay, State Key Laboratory of Wetland Conservation and Restoration, Zhejiang Provincial Key Laboratory of Wetland Intelligent Monitoring and Ecological Restoration, Research Institute of Subtropical Forestry, Chinese Academy of Forestry, Hangzhou 311400, China

*Corresponding author: Niu Li

Address: Research Institute of Subtropical Forestry, Chinese Academy of Forestry, Daqiao Road 73, Hangzhou, Zhejiang, 311400, China

E-mail addresses: Niuli@caf.ac.cn

Tel: +86 0571 63342931

Fax: +86 0571 63342931

Abstract

Tillage- and mulching-based interventions are increasingly used to control invasive plants and modify soil hydro-salinity, but their effects on subsoil carbon (C) stabilization are poorly quantified. We conducted an 18-month field experiment in a Spartina alterniflora–invaded estuarine wetland to compare plastic mulching (PM) and deep tillage (DT) and to resolve microbial–mineral controls on C across the 0–100 cm profile. PM induced pronounced, profile-wide desalinization, with salinity

decreasing by 43–53%. It also redistributed microbial biomass, increasing microbial biomass C in 30–100 cm soils from approximately 25% at 30–50 cm to more than 100% at 50–100 cm. Relative to DT, PM was associated with much larger C depletion, with total C declining by 19–35% and the strongest SOC losses occurring at depth (up to ~65%). Carbon losses co-varied with weakened mineral protection, including 30–50% decreases in poorly crystalline Fe oxides (Feo) and 35–50% reductions in iron-bound organic carbon (Fe–OC). These coupled changes suggest a potential weakening of Fe-mediated protection of subsoil C under rapid desalinization. Depth-resolved partial least squares path modeling suggested contrasting linkages by horizon: surface bacterial community attributes were associated with SOC retention, whereas deep-soil MBC covaried with reactive Fe decline and potential C stock loss. Integrated across 0–100 cm, PM was associated with a potential soil C stock loss of 65 ± 12 Mg C ha^{-1} over 18 months. These results highlight that mulching and tillage practices can have divergent subsoil C outcomes and that reactive Fe–C metrics are valuable for evaluating management impacts beyond the plough layer.

Keywords: Soil organic carbon; Iron-bound carbon; Microbial biomass; Desalinization; *Spartina alterniflora*; Blue carbon

1. Introduction

Coastal wetland soils sequester disproportionate amounts of organic carbon per unit area (up to 200 Mg C ha^{-1} in top meter), with 60-70% stored below 30 cm depth, protected by association with iron minerals and anaerobic conditions (Xia et al., 2022; Hao et al., 2024; Rogers et al., 2019). Invasion by *Spartina alterniflora* (*S.*

alterniflora) has triggered widespread ecological restoration interventions, including mechanical removal and plastic mulching (PM), that fundamentally alter surface hydrology and salinity (Li et al., 2022; Wang et al., 2025a). Yet restoration assessments focus almost exclusively on vegetation recovery and surface soil (0-30 cm) carbon dynamics (Yang et al., 2023; Zhang et al., 2022; Zhang et al., 2023), implicitly assuming that deeper horizons remain biogeochemically inert. This assumption leaves critical questions unanswered: Can management-induced changes in surface hydro-salinity propagate downward and alter subsurface microbial biomass? And if so, what are the consequences for iron-mediated carbon stabilization mechanisms in deep soils?

The long-term stability of wetland soil carbon hinges on iron-organic associations formed under anaerobic conditions, where Fe(III)-reducing bacteria couple organic matter oxidation to iron oxide dissolution, paradoxically both mineralizing and stabilizing carbon depending on redox oscillations (Wang et al., 2022; Yu et al., 2021; Feng et al., 2025). This "Iron Gate" mechanism, wherein organo-Fe complexes resist microbial attack, is particularly prevalent in subsurface horizons where poorly crystalline ferrihydrite and reactive Fe(II) species accumulate (Jia et al., 2022; Wang et al., 2017). Salinity further modulates this system by suppressing microbial metabolic rates through osmotic stress, with halophilic taxa dominating at electrical conductivity >8 dS m^{-1} (Luo et al., 2025; Zhang et al., 2021). Traditional soil science posits that carbon metabolism declines exponentially with depth due to substrate depletion and physical isolation, rendering deep soils (>30 cm)

biogeochemically dormant (Liu et al., 2022; Zheng et al., 2024). However, this paradigm derives largely from terrestrial systems and short-term laboratory incubations. In coastal wetlands, where profile-wide desalinization via freshwater infiltration or management interventions (e.g., PM) can alleviate osmotic constraints, the dormancy assumption remains untested. If deep-soil microbial biomass is partly constrained by osmotic stress, then desalinization may increase subsurface microbial biomass and potentially weaken iron-associated C protection through coupled changes in reactive Fe pools and microbial processes.

Despite the mechanistic understanding of iron-carbon coupling and microbial osmotic stress, three critical knowledge gaps preclude prediction of restoration impacts on deep soil carbon fate. First, nearly all studies of post-restoration biogeochemistry focus on 0-30 cm depth (Xiao et al., 2021; Li et al., 2021; Libbey and Hernández, 2021), leaving subsurface iron dynamics and microbial responses uncharacterized. Second, the spatial extent of desalinization effects, whether localized to mulch-covered surfaces or propagated through entire soil profiles, has not been quantified in field settings. Third, the relative contributions of abiotic iron oxide dissolution versus microbial iron reduction to Fe–OC destabilization remain unresolved, particularly under fluctuating redox-salinity conditions induced by management. Addressing these gaps is essential not only for refining wetland carbon budgets but also for identifying potential carbon costs of restoration that could offset vegetation-based sequestration gains. If common practices such as PM increase deep-soil microbial biomass and weaken Fe-associated C protection, current

restoration assessments may underestimate potential subsoil C vulnerability and carbon-accounting uncertainty.

Here, we conducted a full-profile (0-100 cm) assessment of iron-carbon-microbe dynamics in a *S. alterniflora*-invaded coastal wetland 18 months after implementing two widely used restoration interventions: plastic mulching (PM, targeting moisture retention and weed suppression) and deep tillage (DT, enhancing physical disruption and aeration). We tested three specific hypotheses: (H1) PM-induced desalinization extends beyond surface layers to reduce osmotic stress in deep soils (30–100 cm), enhancing subsurface microbial biomass as an indicator of potential microbial reactivation. (H2) Desalinization is associated with declines in reactive Fe pools and Fe-bound organic carbon, consistent with a potential weakening of Fe-mediated C protection across the profile. (H3) The magnitude of carbon loss correlates with the spatial extent of desalinization and iron destabilization, with profile-wide effects under PM exceeding localized surface impacts under DT. By integrating sequential iron extraction, microbial biomass quantification, bacterial 16S rRNA profiling, and structural equation modeling, this study evaluates potential linkages between restoration-induced environmental changes and deep soil C stability, providing process-based insights for designing climate-smart wetland management strategies.

2. Methods

2.1 Site Description and Experimental Design

The study was conducted in coastal wetlands of southern Hangzhou Bay

(121°52′-121°25′E, 29°39′-30°21′N), Zhejiang Province, China, invaded by *Spartina alterniflora* since 1980s with > 85% coverage (Fig. 1). Soils are classified as typic sulfaquents with mean salinity of 12-18 dS m^{-1} in surface layers. The site experiences irregular semidiurnal tides (mean tidal range 2.5 m) and a subtropical monsoon climate (mean annual temperature 16.4°C, precipitation 1450 mm).

In June 2023, we established a comparative field design including three management states: (1) CK, unremediated *S. alterniflora* stands; (2) PM, complete aboveground vegetation removal followed by coverage with 0.1 mm black polyethylene film to suppress regrowth and reduce evaporative salt accumulation; and (3) DT, complete aboveground vegetation removal followed by mechanical deep tillage to 160 cm using a rotary cultivator to enhance soil aeration and physical disturbance. Within each management state, five independent 20 m × 20 m sampling plots were established as plot-level replicates, resulting in 15 plots in total. Plots were separated by at least 50 m to minimize spatial dependence and edge effects. This design compared field management states rather than isolating the independent effects of vegetation removal from the subsequent mulching or tillage intervention.

In December 2024, soil sampling was conducted 18 months after treatment implementation. Within each 20 m × 20 m plot, five soil cores were collected, including one at the plot center and four in the cardinal directions 5 m from the center. Each core was segmented into five depth intervals: 0–10, 10–20, 20–30, 30–50, and 50–100 cm. For each plot, cores from the same depth were homogenized to form one composite sample, yielding 75 composite samples in total (3 management states × 5

plots × 5 depths). Samples were immediately transported to the laboratory on ice and divided into three aliquots: (i) fresh soil stored at 4°C for physicochemical and iron analyses (<2 mm sieving); (ii) air-dried soil (25°C, <0.25 mm) for total C/N and Fe–OC analyses; and (iii) frozen soil (-80°C) for DNA extraction.

2.2 Soil Physicochemical Analyses

Soil pH and electrical conductivity (EC) were measured in 1:5 (w/v) soil-to-deionized water suspensions after 30 min end-over-end shaking at 25°C, using a glass electrode pH meter (PHSJ-3F, INESA, Shanghai, China) and conductivity meter (DDS-307, INESA), respectively. Gravimetric soil moisture was determined by oven-drying at 105°C for 24 h. Soil bulk density was measured using intact cores (100 cm^3) collected adjacent to sampling points, dried at 105°C, and weighed. Soil inorganic nitrogen (NH_4^+ and NO_3^-) was extracted from 5 g fresh soil with 50 mL of 2 M KCl by shaking at 200 rpm for 1 h at 25°C, followed by filtration (Whatman No. 42). Extracts were analyzed colorimetrically using a continuous-flow analyzer (AA3, SEAL Analytical, Germany) . Total carbon (TC) and nitrogen (TN) were determined using an elemental analyzer (Vario MAX CN, Elementar, Germany). Soil organic carbon (SOC) was estimated by loss-on-ignition (LOI) at 550°C for 4 h. LOI-derived SOC was used as an operational estimate of organic C and interpreted separately from elemental-analyzer-derived TC. We therefore used TC and SOC as complementary C metrics rather than directly interchangeable measurements. Microbial biomass carbon (MBC) and nitrogen (MBN) were quantified using the chloroform

fumigation-extraction method (Oren et al., 2018). Paired fresh soil samples (8 g, n=3 analytical replicates per composite) were either fumigated with ethanol-free chloroform in a vacuum desiccator for 24 h at 25°C or left non-fumigated. Both sets were extracted with 40 mL of 0.5 M K_2SO_4 by shaking for 30 min at 200 rpm, followed by centrifugation (4000 rpm, 10 min) and filtration (0.45 μm nylon). Organic C and total N in extracts were analyzed using a TOC/TN analyzer (TOC-L, Shimadzu, Japan). MBC and MBN were calculated as: MBC = EC / kEC and MBN = EN / kEN, where EC and EN are the differences in extracted C and N between fumigated and non-fumigated samples, and kEC = 0.45 and kEN = 0.54 are extraction efficiency factors (Joergensen, 1996; Brookes et al., 1985).

2.3 Iron Fractionation and Fe-bound Organic Carbon

Soil iron (Fe) pools were sequentially extracted following modified procedures of Poulton and Canfield (2005). Free Fe oxides (Fed, primarily crystalline hematite and goethite) were extracted by adding 40 mL of citrate-bicarbonate-dithionite (CBD) solution (0.27 M sodium citrate, 0.11 M sodium bicarbonate, 1 g sodium dithionite) to 1 g soil, heated in an 80°C water bath for 15 min with occasional stirring. Amorphous Fe oxides (Feo, mainly ferrihydrite and lepidocrocite) were extracted with 40 mL of 0.2 M ammonium oxalate/0.17 M oxalic acid (pH 3.0) in the dark at 25°C for 4 h with continuous end-over-end shaking. Organically complexed Fe (Fep) was extracted with 40 mL of 0.1 M sodium pyrophosphate (pH 10) by shaking for 16 h at 25°C. After each extraction, samples were centrifuged (4000 rpm, 10 min), and supernatants were

filtered (0.45 μm) and acidified with 2% HNO_3 for storage. Iron concentrations in extracts were determined by inductively coupled plasma optical emission spectrometry (ICP-OES; iCAP 7400, Thermo Fisher Scientific, USA).

Fe-bound organic carbon (Fe–OC) was determined following Wagai and Mayer (2007) with modifications. Briefly, duplicate 1 g soil samples were treated with 40 mL of CBD solution (same composition as Fed extraction) at 25°C for 8 h in the dark to reductively dissolve Fe oxides and release associated OC. Control samples received 40 mL of 1 M NaCl solution (equivalent ionic strength) to account for OC loss via dispersion without Fe dissolution. After extraction, residues were washed three times with deionized water, freeze-dried, and ground to <0.25 mm. Organic C content in residues was measured using the elemental analyzer (Vario MAX CN). Fe–OC was calculated as:

$$\text{Fe–OC (g kg}^{-1}) = \text{OC\_control} - \text{OC\_CBD} \quad (1)$$

where OC_control and OC_CBD are organic carbon concentrations in control and CBD-treated residues, respectively. The proportion of Fe-associated OC ($f_{Fe–OC}$, %) was calculated as (Fe–OC / SOC) × 100.

2.4 Microbial Community Structure

Total genomic DNA was extracted from 0.5 g frozen soil using the E.Z.N.A.® Soil DNA Kit (Omega Bio-tek, USA) following manufacturer instructions. DNA quality was assessed by 1.0% agarose gel electrophoresis with GelRed staining, and concentration/purity were determined using a NanoDrop 2000 spectrophotometer

(Thermo Fisher Scientific). The V4 hypervariable region of bacterial 16S rRNA gene was amplified using primers 515F (5′-GTGYCAGCMGCCGCGGTAA-3′) and 806R (5′-GGACTACNVGGGTWTCTAAT-3′). PCR reactions (25 μL) contained 12.5 μL 2× Phusion High-Fidelity PCR Master Mix (New England Biolabs), 0.5 μM each primer, and 20 ng template DNA. Amplification was performed in a T100 Thermal Cycler (Bio-Rad) using: initial denaturation at 95°C for 3 min; 27 cycles of 95°C for 30 s, 55°C for 30 s, 72°C for 30 s; final extension at 72°C for 10 min. Three technical replicates per sample were pooled, purified using the AxyPrep DNA Gel Extraction Kit (Axygen), and quantified by Qubit 4.0 Fluorometer (Invitrogen). Equimolar amounts (100 ng per sample) were pooled and sequenced on an Illumina MiSeq platform (2 × 300 bp paired-end) by Majorbio Bio-Pharm Technology Co. (Shanghai, China), targeting >50,000 raw reads per sample.

Raw sequences were processed using QIIME2 (v2022.11). Primers were removed with cutadapt (v4.1), and reads were quality-filtered (Q > 20), denoised, and merged using DADA2 with default parameters. Chimeric sequences were identified and removed using VSEARCH (v2.21.1). Amplicon sequence variants (ASVs) were taxonomically assigned using the SILVA database (v138, 99% similarity threshold). Samples were rarefied to 40,000 sequences per sample to normalize sequencing depth. ASVs classified as chloroplasts, mitochondria, or unassigned at domain level were excluded from downstream analyses.

2.5 Soil Organic Carbon Stock Calculations

SOC stocks were calculated using the fixed-depth (FD) approach following previous studies (Wendt and Hauser, 2013; Peng et al., 2024). Because management practices, particularly deep tillage, may alter bulk density and soil mass, these estimates should be interpreted as fixed-depth comparisons rather than equivalent-soil-mass-corrected stock estimates. The fixed-depth SOC stock (SOCS_FD, Mg C ha^{-1}) for each layer was:

$$SOCS\_FD_i = SOC_i \times BD_i \times D_i \times 0.1 \quad (2)$$

where SOC_i is organic carbon concentration (g kg^{-1}), BD_i is bulk density (g cm^{-3}), and D_i is layer thickness (cm) for the ith layer. The constant 0.1 converts units to Mg C ha^{-1}.

2.6 Statistical Analyses

All data were tested for normality (Shapiro-Wilk test) and homogeneity of variance (Levene's test) prior to parametric analyses. When necessary, data were log or square root-transformed to meet assumptions. Effects of treatment and depth on individual variables (soil properties, iron pools, Fe–OC, microbial biomass, α-diversity indices) were assessed using two-way analysis of variance (ANOVA) with treatment and depth as fixed factors. Post-hoc pairwise comparisons were conducted using Duncan's test at $\alpha = 0.05$. All univariate analyses were performed in SPSS (v27.0, IBM Corp.). Bacterial community β-diversity was calculated using Bray-Curtis dissimilarity based on Hellinger-transformed ASV relative abundances to reduce the influence of rare taxa. Principal coordinates analysis (PCoA) was used for

visualization, and treatment effects were tested using permutational multivariate analysis of variance (PERMANOVA) with 999 permutations. Relationships between microbial community structure and environmental variables were examined using Mantel tests (Spearman's correlation, 999 permutations). Pairwise Pearson correlations between dominant bacterial phyla and soil properties were calculated and visualized as heatmaps. All multivariate analyses were conducted in R (v4.3.1) using vegan (v2.6-4) and ggplot2 (v3.4.2) packages. Partial least squares path modeling (PLS-PM) was used to explore hypothesized direct and indirect associations among management treatments, soil physicochemical properties, reactive Fe pools, microbial variables, and carbon fractions. Path coefficients (β) were estimated using the pls-pm package (v0.4.9) with centroid weighting scheme and 1000 bootstrap iterations for significance testing. Model fit was evaluated using standardized root mean square residual (SRMR < 0.08) and Goodness of Fit (GoF > 0.70) as adequacy thresholds (Henseler et al., 2016). Separate models were constructed for surface (0-20 cm) and deep (30-100 cm) soils to examine depth-dependent mechanisms. All figures were created using Origin Pro (2025, Origin Lab Corp.) and assembled in Adobe Illustrator (2024, Adobe Inc.). Statistical significance was declared at $P < 0.05$ unless otherwise stated, and data are presented as mean ± standard deviation (SD).

3. Results

3.1 Soil hydro-chemical properties and microbial biomass across depths

PM markedly altered soil hydro-chemical conditions across the 0–100 cm profile

(Fig. 2). Soil moisture was significantly affected by treatment, depth, and their interaction ($P < 0.05$; Fig. 2a), and was generally lower under PM than under CK and DT, particularly in the 0–30 cm and 50–100 cm layers. Soil pH showed significant treatment and depth effects ($P < 0.01$), but the treatment × depth interaction was not significant ($P = 0.087$; Fig. 2b). EC and salinity displayed similar patterns, with significant treatment, depth, and interaction effects ($P < 0.05$; Fig. 2c, d). PM produced the lowest EC and salinity throughout the profile, reducing EC and salinity by approximately 55–60% and 54–59%, respectively, in deep soils (30–100 cm) compared with CK.

Nitrogen pools also showed treatment-specific responses (Fig. 2e–g). TN was significantly affected by treatment, depth, and their interaction ($P < 0.001$; Fig. 2e), with PM causing the greatest TN reduction across the profile, declining by 51–74% relative to CK. NH_4^+ showed no significant overall treatment, depth, or interaction effects according to two-way ANOVA ($P > 0.05$; Fig. 2f), although its distribution varied among treatments at individual depths. NO_3^- was significantly affected by treatment ($P < 0.001$), but the effects of depth and treatment × depth interaction were marginally non-significant ($P = 0.056$ and $P = 0.058$, respectively; Fig. 2g). Overall, NO_3^- was highest under CK, lowest under DT, and intermediate under PM.

Microbial biomass C and N were both significantly affected by treatment, depth, and their interaction ($P < 0.001$; Fig. 2h, i). PM significantly reduced MBC in surface soils (0–30 cm; $P < 0.05$), but increased MBC in deep soils (30–100 cm), with the increase ranging from approximately 25% at 30–50 cm to more than 100% at 50–100

cm relative to CK (Fig. 2h). This pattern indicates a shift in the vertical distribution of microbial biomass under PM. In contrast, DT reduced surface salinity by approximately 20% ($P < 0.05$; Fig. 2c, d), but had limited effects on deep-soil salinity and was associated with 9–45% lower MBC across the profile ($P < 0.05$; Fig. 2h). MBN generally declined with soil depth in all treatments, while DT and PM showed higher MBN than CK in most soil layers ($P < 0.05$; Fig. 2i).

3.2 Soil carbon pools and iron-associated carbon fractions

TC was significantly affected by treatment, depth, and their interaction ($P < 0.01$; Fig. 3a). Across the 0–100 cm profile, TC was generally highest under CK and lowest under PM, with DT showing intermediate values. Relative to CK, PM reduced TC by approximately 19–35%, whereas DT caused smaller decreases. SOC showed a significant treatment effect ($P < 0.001$), while depth and treatment × depth interaction were not significant ($P = 0.931$ and $P = 0.314$, respectively; Fig. 3b). SOC generally followed the order CK > DT > PM, with PM reducing SOC by approximately 34–65% across the profile.

Fe–OC showed a similar treatment-dependent pattern ($P < 0.001$), whereas depth and treatment × depth interaction were not significant ($P = 0.814$ and $P = 0.615$, respectively; Fig. 3c). PM consistently showed lower Fe–OC than CK and DT, with reductions of approximately 35–50% relative to CK. This decline co-occurred with lower reactive Fe pools, suggesting a potential weakening of Fe-mediated C protection under PM. SOCS-FD was significantly affected by treatment and depth (P

300 < 0.01 and $P < 0.001$, respectively), but not by their interaction ($P = 0.504$; Fig. 3d).
301 In the 0–50 cm layers, SOCS-FD generally followed CK > DT > PM, whereas all
302 treatments showed the highest SOCS-FD in the 50–100 cm layer.

303 Reactive Fe fractions showed significant treatment effects (Fig. 3e–g). Fep was
304 significantly affected by treatment ($P < 0.01$), but not by depth or treatment × depth
305 interaction ($P = 0.317$ and $P = 0.291$, respectively; Fig. 3e). Fep was relatively higher
306 under PM in the upper soil layers, but this pattern weakened at depth. Fed and Feo
307 were also significantly affected by treatment ($P < 0.001$), with no significant depth or
308 interaction effects ($P > 0.05$; Fig. 3f, g). PM generally reduced Fed and Feo relative to
309 CK, with Feo decreasing by approximately 30–50%. The proportion of Fe–OC to
310 SOC, $f_{Fe\text{-}OC}$, was significantly affected by treatment ($P < 0.05$), but not by depth or
311 treatment × depth interaction ($P = 0.920$ and $P = 0.290$, respectively; Fig. 3h). $f_{Fe\text{-}OC}$
312 tended to be higher under PM and DT than under CK in the upper soil layers, whereas
313 treatment differences were weaker in deeper soils.

314 **3.3 Bacterial community composition and diversity**

315 PCoA revealed significant treatment-induced differentiation of bacterial
316 community structure. At 0-10 cm depth, communities exhibited clear separation
317 (PERMANOVA: $R^2 = 0.465$, $P < 0.001$; Fig. S1), with PM samples diverging from
318 CK and DT along PC1 (explaining 28.48% of variance) and CK separating from DT
319 along PC2 (23.49% of variance). Community differentiation intensified at 10-20 cm
320 depth (PERMANOVA: $R^2 = 0.605$, $P < 0.001$), where treatments formed distinct

clusters in multivariate space defined by PC1 (25.61%) and PC2 (21.06%).

Alpha diversity metrics tended to be lower under PM at 0–10 cm and 10–20 cm, but the differences were not statistically significant ($P > 0.05$; Table S1). Venn diagram analysis identified 652 core amplicon sequence variants (ASVs) shared among all treatments at 0-10 cm, alongside treatment-specific ASVs numbering 3,482 (PM), 2,953 (CK), and 3,009 (DT; Fig. 4a). At 10-20 cm depth, 613 core ASVs were shared, with 3,400 (CK), 3,151 (DT), and 3,228 (PM) unique ASVs (Fig. 4b).

At the genus level, surface soil (0-10 cm) bacterial assemblages displayed treatment-specific taxonomic signatures. CK soils harbored elevated relative abundances of *Sulfurifustis* and *Acidibacter*, DT soils were enriched in *Nocardioides, unclassified Gemmatimonadaceae*, and *Nitrospira*, while PM soils were characterized by *Thiobacillus*, *Subgroup_22*, and *unclassified MBNT15 taxa*. At 10-20 cm depth, these patterns persisted, with additional increases in the relative abundances of *BD2-11 terrestrial group*, *Gammaproteobacteria*, and *Desulfobacterota* observed in both DT and PM treatments (Fig. 4c, d). Circos plots visualized broader taxonomic band widths and denser cross-sample connections for dominant genera in PM treatments, indicating enhanced community complexity (Fig. 4c, d)

3.4 Relationships between environmental factors and carbon dynamics

Mantel tests revealed strong, depth-dependent correlations between bacterial community structure and environmental factors (Fig. 5a-b). In surface soils (0–20 cm), salinity/electrical conductivity (SAL/EC) and Fe–C-related variables (SOC, TC, MBC,

TN, fFe–OC, Feo, and Fed) were the main correlates of community variation ($r \geq 0.4$, $P < 0.01$), with SOC, TC, and $f_{Fe–OC}$ showing strong positive inter-correlations ($r \approx 0.8–1.0$) and negative correlations with NO_3^-. Soil moisture and pH had weaker effects, particularly at 0-10 cm, but their influence increased at 10-20 cm. RDA corroborated these findings, explaining 74.73% of community variation at 0-10 cm, with PM samples distinctly separated along RDA1, driven by high pH and Fep versus low SOC, TC, and f_{Fe-OC} (Fig. S2).PLS-PM suggested hypothesized associations among management, soil physicochemical conditions, reactive Fe pools, microbial variables, and C fractions (GoF = 0.729; Fig. 5c, d). PM was strongly associated with altered soil physicochemical conditions ($\beta = -0.854$, $P < 0.001$), which were negatively associated with Fed ($\beta = -0.344$, $P < 0.01$) and active Fe phases (Fep/Feo, $\beta = -0.312$, $P < 0.05$). These associations were consistent with the observed decreases in SOC ($R^2 = 0.787$) and Fe–OC ($R^2 = 0.610$), but should not be interpreted as direct evidence of causal pathways. In surface soils (0–20 cm), bacterial community attributes were associated with SOC and Fe–OC (Fig. 5e, f), suggesting potential microbial involvement in C–Fe coupling.

4. Discussion

4.1 Profile-wide desalinization was associated with increased deep-soil microbial biomass

Our findings suggest that deep coastal wetland soils (>30 cm) can show measurable microbial and biogeochemical responses to management-induced hydro-salinity changes (Wu et al.,2025b). In our 18-month field study, PM was

associated with profile-wide desalinization and increased MBC in deep soils, suggesting that reduced salinity may relax osmotic constraints on microbial biomass in subsurface horizons.

PM induced substantial reductions in salinity and EC throughout the 0–100 cm profile, with salinity decreasing by 43–53% and EC by 45–50% (Fig. 2c, d), indicating a profile-wide shift in the hydro-chemical environment. Because salinity can constrain microbial biomass and metabolism in saline soils (Huang et al., 2021; Zhang et al., 2024; Wang et al., 2025b), this desalinization may have reduced osmotic limitation and was associated with increased MBC in deep soils, ranging from approximately 25% at 30–50 cm to more than 100% at 50–100 cm relative to CK (Fig. 2h). At the same time, PM reduced MBC in surface soils (0–30 cm), indicating a redistribution of microbial biomass from surface-dominated to relatively deeper horizons. This pattern contrasted with DT, which was associated with lower MBC across most depths and showed limited effects on deep-soil salinity, suggesting that the increase in deep-soil MBC under PM was more closely linked to profile-wide desalinization than to physical disturbance alone.

These results are consistent with studies showing that salinity reduction and other environmental shifts can alter microbial biomass, community structure, and potential functions in saline or coastal wetland soils (Huang et al., 2021; Hernandez et al., 2021). However, bacterial sequencing was conducted only for the 0–10 and 10–20 cm layers. Therefore, the observed increase in deep-soil MBC should be interpreted as evidence of increased microbial biomass rather than direct evidence of changes in

deep-layer bacterial community composition or function. Future depth-resolved sequencing, metagenomics, and activity assays are needed to determine whether similar community or functional shifts occur in the 30–100 cm layers.

If similar increases in deep-soil microbial biomass occur under desalinization-based management in other coastal wetlands, assessments restricted to surface soils may underestimate subsoil C vulnerability (Wen et al., 2023; Chen et al., 2018). Our results support the need for full-profile monitoring, including at least the upper 1 m of soil, when evaluating restoration effects on subsoil C stability in saline coastal wetlands.

4.2 Coupled C and N responses under post-removal management

The concurrent declines in C and N pools indicate that PM altered sediment nutrient stoichiometry as well as C storage. In addition to the 19–35% decline in TC and 34–65% decline in SOC, PM caused a 51–74% reduction in TN and altered the vertical distributions of NH_4^+ and NO_3^-. Such coordinated C–N responses are consistent with evidence that coastal wetland restoration affects soil C and N recovery simultaneously, and that salinity gradients can reshape the sources and decomposition status of estuarine wetland soil organic matter through changes in C:N ratios and isotopic signals (Xia et al., 2021; Chen et al., 2026). These coordinated changes suggest that C depletion under PM was accompanied by a broader reorganization of sediment nutrient availability.

406 Changes in inorganic N availability may influence microbial biomass and
407 organic matter decomposition by modifying microbial nutrient demand, C:N balance,
408 and resource acquisition strategies. In coastal estuarine wetlands, salinity has been
409 shown to regulate microbial community structure and functional potential, while
410 Spartina alterniflora can strongly alter gross N transformation pathways, including
411 mineralization, immobilization, and nitrification (Zhang et al., 2021; Chen et al.,
412 2022). More generally, microbial C:N stoichiometry and nutrient availability can
413 regulate microbial biomass turnover, enzyme allocation, and priming effects during
414 organic matter decomposition (Chen et al., 2019; Zhu et al., 2021). In coastal wetland
415 sediments, changes in organic resource availability can also reshape microbial
416 community structure and greenhouse gas production potential (Lin and Lin, 2022).
417 Therefore, reduced TN under PM may intensify microbial N limitation, whereas
418 changes in NH_4^+ and NO_3^- availability may alter the balance among mineral N uptake,
419 organic matter decomposition, and microbial growth. However, because rates of N
420 mineralization, nitrification, denitrification, DNRA, and microbial assimilation were
421 not measured, the present data cannot identify the specific N transformation pathways
422 responsible for the observed inorganic N patterns. We therefore interpret the N
423 responses as coupled indicators of sediment biogeochemical reorganization rather
424 than direct evidence of altered N cycling processes.

425 **4.3 Reactive Fe decline and potential weakening of Fe-mediated C protection**

426 The declines in C pools under PM, including 19–35% lower TC and 34–65%

lower SOC, co-occurred with reduced Fe–OC across the 0–100 cm profile (Fig. 3a–c). Because Fe–organic associations are important for long-term C preservation in anaerobic wetland soils, these coupled changes suggest a potential weakening of Fe-mediated C protection (Wu et al., 2025a; Ni et al., 2024). PM was associated with 30–50% lower poorly crystalline Feo and 35–50% lower Fe–OC than CK, with generally stronger reductions than those observed under DT (Fig. 3c, g). These patterns may reflect several, non-mutually exclusive pathways involving changes in Fe mobility, microbial C turnover, and hydrological export.

Geochemically, profile-wide desalinization may have altered the solubility and mobility of reactive Fe phases through changes in ionic strength and pH, potentially affecting Fe–organic associations under anaerobic conditions (Wang et al., 2025c; Yang et al., 2021). The decline in Feo, a highly reactive Fe fraction, is consistent with a reduction in the soil capacity to retain Fe–associated organic C (Fig. 3g). Biologically, microbial Fe reduction can couple Fe(III) reduction to organic C oxidation in anaerobic sediments (Lovley and Phillips, 1988; Zhao et al., 2025). However, our study did not directly measure Fe-reducing activity, Fe(II)/Fe(III) speciation, or deep-layer bacterial community composition. Therefore, increased deep-soil MBC should be interpreted as potential microbial involvement in C–Fe coupling rather than direct evidence of microbial Fe reduction. The PLS-PM results were consistent with this hypothesized pathway, showing that PM-associated physicochemical changes were negatively associated with reactive Fe pools and C fractions (Fig. 5c, d). However, these path relationships should be interpreted as

449 exploratory associations rather than direct causal evidence. Alternative mechanisms
450 should also be considered. Fe–OC declines could reflect leaching of dissolved
451 Fe(II)–organic complexes after Fe mobilization rather than complete mineralization to
452 CO_2 (Daugherty et al., 2017). Because we did not measure pore-water DOC,
453 Fe(II)/Fe(III) speciation, CO_2 or CH_4 fluxes, or lateral hydrological export, we cannot
454 determine whether the observed Fe–OC decline resulted primarily from microbial
455 mineralization, dissolved export, or within-profile redistribution. Thus, the observed
456 C and Fe–OC declines should be interpreted as evidence of potential C destabilization
457 rather than confirmed atmospheric C emissions.

458 Depth-stratified PLS-PM models suggested contrasting microbial-C associations
459 between surface and deep soils. In surface soils (0–20 cm), bacterial community
460 attributes were associated with SOC and $f_{Fe\text{-}OC}$ (Fig. 5e, f), possibly reflecting the
461 involvement of sulfur- and Fe-related taxa such as *Thiobacillus* and *Desulfobacterota*
462 in anaerobic or microaerobic C-Fe cycling (Berg et al., 2019). In deep soils (30–100
463 cm), lower salinity, increased MBC, and reduced reactive Fe pools covaried with
464 lower SOC and Fe–OC, indicating depth-dependent associations among
465 hydro-salinity, microbial biomass, and Fe-mediated C protection. Notably, DT
466 maintained 10-22% higher $f_{Fe\text{-}OC}$ than PM in the upper 0–50 cm layers (Fig. 3h),
467 suggesting that physical disturbance without profile-wide desalinization may have a
468 weaker effect on Fe-associated C protection than PM. This distinction highlights that
469 the magnitude and spatial extent of hydro-geochemical change may be more
470 important than disturbance intensity alone in regulating Fe-C coupling after *S.*

alterniflora management.

4.4 Implications for restoration C assessment: potential destabilization rather than confirmed emissions

Evaluating the C implications of wetland restoration requires integrating soil stock changes, vegetation recovery, and flux-based C pathways over appropriate timescales. The fixed-depth stock estimate indicated an apparent soil C stock decline of 65 ± 12 Mg C ha^{-1} across the 0–100 cm profile under PM during the 18-month post-treatment period. As a contextual comparison, aboveground biomass C in restored coastal wetlands often accumulates at approximately 1–3 Mg C ha^{-1} yr^{-1} following native vegetation re-establishment (Zheng et al., 2025; Rowland et al., 2024). This comparison highlights that short-term subsoil C changes may be large relative to early vegetation C gains, but a true offset calculation would require long-term measurements of vegetation biomass, soil C trajectories, and C fluxes.

These observations raise uncertainty about short-term restoration C balance, particularly if PM-associated soil C stock declines persist beyond the initial 18-month period. Three trajectories remain possible: (1) stabilization as labile C pools are depleted; (2) deceleration if recovering vegetation enhances C inputs and soil aggregation; or (3) continued decline if reduced Fe–OC protection and altered hydro-salinity conditions persist. Without multi-year monitoring and direct measurements of CO_2 and CH_4 fluxes, pore-water DOC, and lateral hydrological export, we cannot determine whether PM-treated sites function as net atmospheric C

492 sources or whether part of the depleted soil C was redistributed or exported in
493 dissolved forms.

494 Our findings are consistent with growing evidence that restoration interventions
495 can alter legacy soil C stocks and create potential short-term C costs that may offset
496 early vegetation-based C gains (Ascenzi et al., 2025; Bhan et al., 2025; Lin et al.,
497 2025). Given the broad distribution of *S. alterniflora*-invaded wetlands in eastern
498 China, the spatial variability of post-removal soil C responses deserves further
499 regional assessment.

500 These results highlight the need to broaden restoration C assessment frameworks.
501 Current blue carbon assessments often emphasize vegetation biomass and surface
502 soils (0–30cm), potentially overlooking subsoil C vulnerability and
503 mineral-associated C dynamics (Murdiyarso et al., 2023; Asanopoulos et al., 2021).
504 We therefore suggest that restoration C assessments incorporate: (1) full-profile soil C
505 monitoring, at least to 1 m depth; (2) Fe-associated C metrics, including Fe–OC and
506 $f_{Fe\text{-}OC}$, as indicators of mineral-associated C vulnerability; and (3) multi-year
507 measurements of gaseous and dissolved C fluxes to resolve whether stock changes
508 represent mineralization, lateral export, or redistribution.

509 **4.5 Limitations and future research**

510 Several limitations of this study should guide future research. First, our
511 18-month dataset captures only the initial response to post-removal management.
512 Multi-year monitoring is needed to determine whether the observed C stock declines

stabilize, decelerate, or reverse as vegetation recovery, hydrological conditions, and sediment biogeochemistry develop over time. This temporal caution is particularly important because ecosystem C and N recovery in restored coastal wetlands can require decades, and soil C and N pools often recover more slowly than vegetation biomass (Chen et al., 2026).

Second, our experimental design compared integrated field management states rather than fully isolated single-factor treatments. CK represented unremediated *S. alterniflora* stands, whereas PM and DT both involved complete vegetation removal followed by a post-removal intervention. Therefore, contrasts between CK and the two managed treatments include both vegetation removal and subsequent management effects. Nevertheless, because vegetation removal was common to PM and DT, their comparison provides insight into divergent belowground responses to two post-removal strategies. Treatment differences should therefore be interpreted as responses to field management states rather than as fully isolated effects of mulching or tillage alone.

Third, the absence of direct CO_2 and CH_4 flux measurements, pore-water DOC data, Fe(II)/Fe(III) speciation, and measurements of lateral hydrological export prevents us from resolving the fate of the decreased soil C pool. Future studies should combine depth-resolved greenhouse gas flux monitoring with pore-water C and Fe chemistry to distinguish microbial mineralization, dissolved Fe–organic export, and within-profile redistribution. This is important because restored coastal wetlands can export substantial dissolved and gaseous C through surface water and groundwater

pathways, including DOC, DIC, CO_2, and CH_4 (Sadat-Noori et al., 2024).

Fourth, our single-site study in Hangzhou Bay may not be directly generalizable to other coastal wetlands with different baseline salinity, tidal regimes, vegetation types, sediment texture, or management histories. Comparative studies across regional salinity and hydrological gradients are needed to identify the conditions under which post-removal management may increase subsoil C vulnerability.

Mechanistically, the microbial functional potential underlying deep-soil C turnover and Fe transformation remains unresolved. Depth-resolved metagenomic and metatranscriptomic approaches targeting Fe-reduction genes, organic C depolymerization pathways, and respiratory metabolisms could help identify the microbial groups and functional traits potentially involved in C–Fe coupling. Such approaches have been used to infer the genetic potential for microbial Fe redox cycling in sedimentary environments (Garber et al., 2021). Complementary measurements of depth-resolved redox potential, Fe(II)/Fe(III) speciation, microbial respiration, and Fe-reduction rates would allow explicit testing of the hypothesized C–Fe–microbe linkages.

Finally, translating site-specific observations into predictive capacity requires process-based modeling. Incorporating osmotic stress responses, reactive Fe dynamics, microbial biomass and process rates into models such as Wetland-DNDC and DAYCENT would enable scenario analysis of restoration strategies under varying environmental conditions. Process-based models such as DNDC and DayCent have

been evaluated for wetland and blue-carbon applications, but their reliability depends on adequate representation of hydrology, soil C dynamics, vegetation recovery, and greenhouse gas fluxes (Mack et al., 2023). Such models could help evaluate management options that balance invasive species control with subsoil C preservation, such as staged post-removal interventions or strategies that avoid rapid profile-wide hydro-salinity shifts.

5. Conclusion

In this 18-month field study, post-removal plastic mulching was associated with strong profile-wide desalinization and a pronounced reorganization of soil C pools and Fe-associated C dynamics across the 0–100 cm profile. Compared with deep tillage, plastic mulching coincided with greater C depletion, with TC declining by 19–35% and SOC declining by up to 65%, particularly in deeper horizons. Deep soils (30–100 cm) showed a 25–110% increase in MBC, indicating a redistribution of microbial biomass toward deeper horizons under desalinized conditions. These C changes co-occurred with reduced mineral-associated protection, as indicated by coupled declines in poorly crystalline Fe oxides (Feo; 30–50%) and Fe-bound organic carbon (Fe–OC; 35–50%). Depth-resolved path modeling further suggested horizon-specific associations: surface bacterial community attributes were associated with SOC retention, whereas deep-soil MBC covaried with reactive Fe decline and lower SOC. Integrated across the 0–100 cm profile, plastic mulching was associated with an apparent fixed-depth soil C stock decline of 65 ± 12 Mg C ha^{-1} over 18 months. Overall, these findings suggest that post-removal mulching and deep tillage

can lead to contrasting subsoil C outcomes, highlighting the need for profile-resolved monitoring and reactive Fe–C metrics when evaluating coastal wetland restoration beyond the surface layer.

Figures

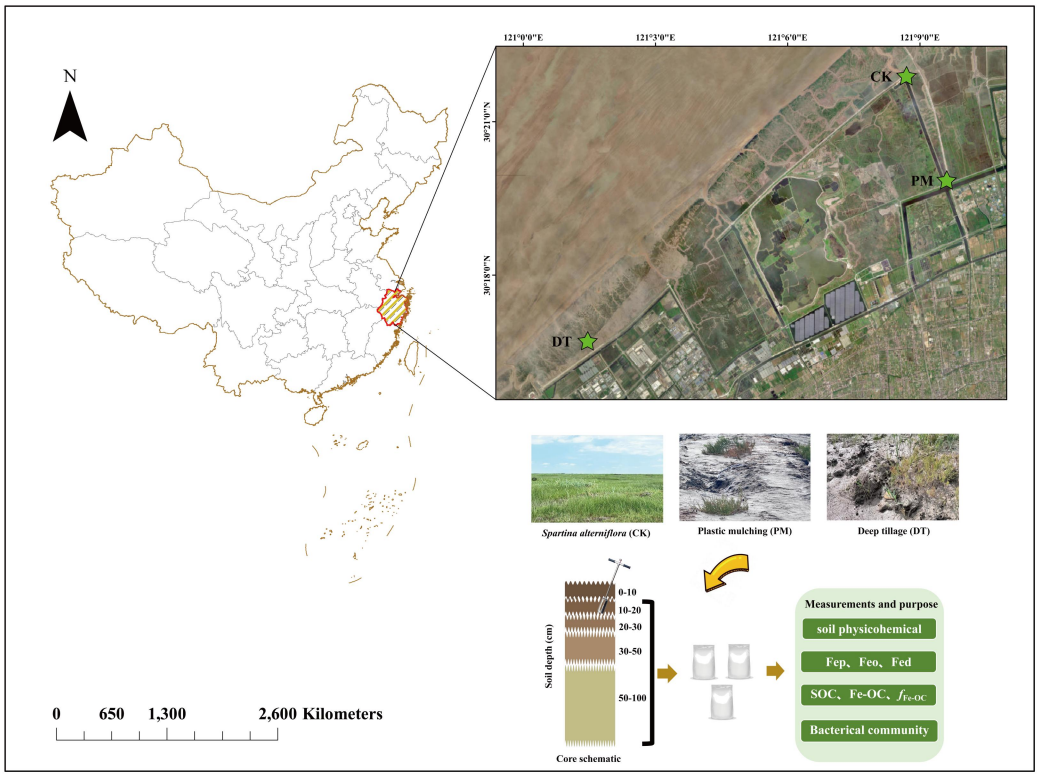

Fig. 1 Geographic location and schematic sampling design of the study area in the coastal wetlands of Hangzhou Bay, Zhejiang Province, China. The map shows representative areas for the three field management states: CK, unremediated *S. alterniflora* stands; PM, *S. alterniflora* removal followed by plastic mulching; and DT, *S. alterniflora* removal followed by deep tillage. Within each management state, five independent 20 m × 20 m sampling plots were established as plot-level replicates. The five replicate plots within each management state are not individually shown. Basemap/satellite imagery was obtained from Tianditu (National Platform for Common Geospatial Information Services, China), accessed on 25 September 2025.

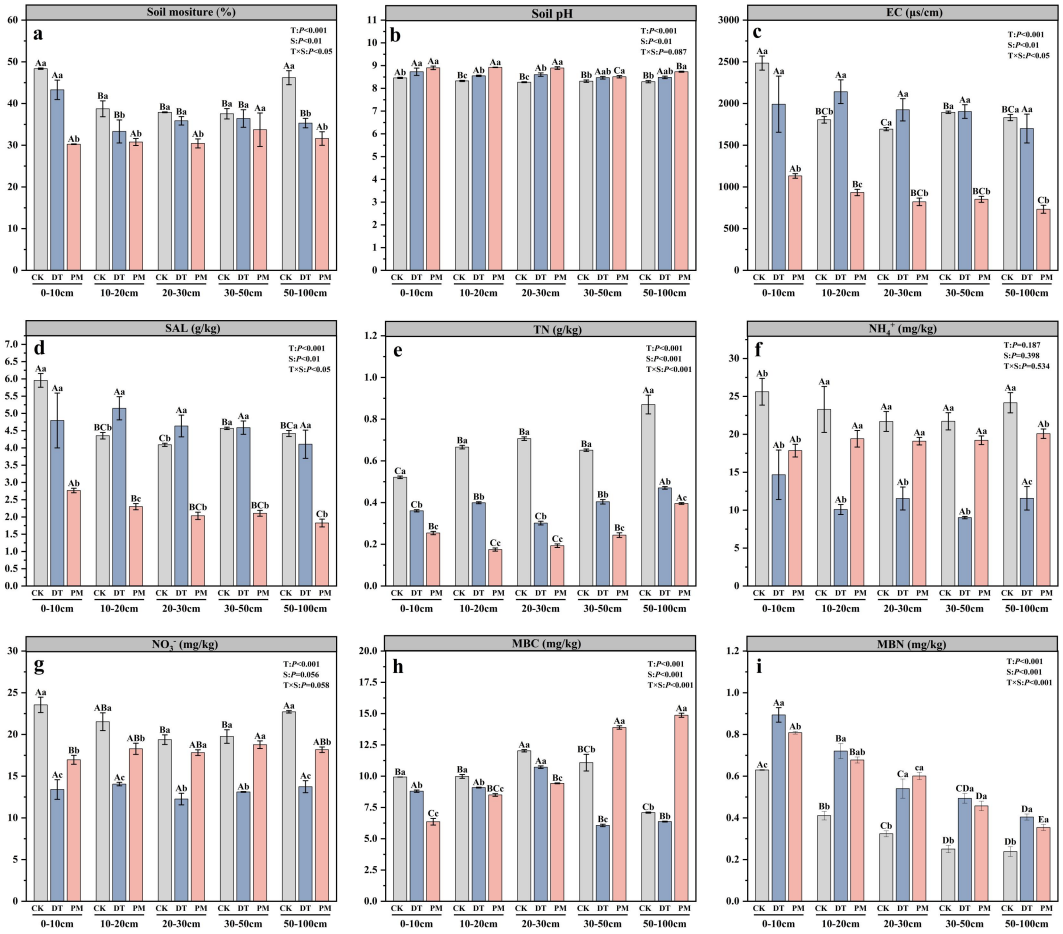

Fig. 2 Soil physicochemical properties under different management treatments. (a) Soil moisture, (b) pH, (c) electrical conductivity (EC), (d) salinity (SAL), (e) total nitrogen (TN), (f) ammonium (NH_4^+), (g) nitrate (NO_3^-), (h) microbial biomass carbon (MBC), and (i) microbial biomass nitrogen (MBN) across soil profiles under CK (control), DT (deep tillage), and PM (plastic mulching) treatments. Bars represent the mean ± standard error, and lowercase letters above the bars indicate significant differences between treatments at the same soil depth ($P < 0.05$), while uppercase letters indicate significant differences between soil depths within the same treatment ($P < 0.05$).

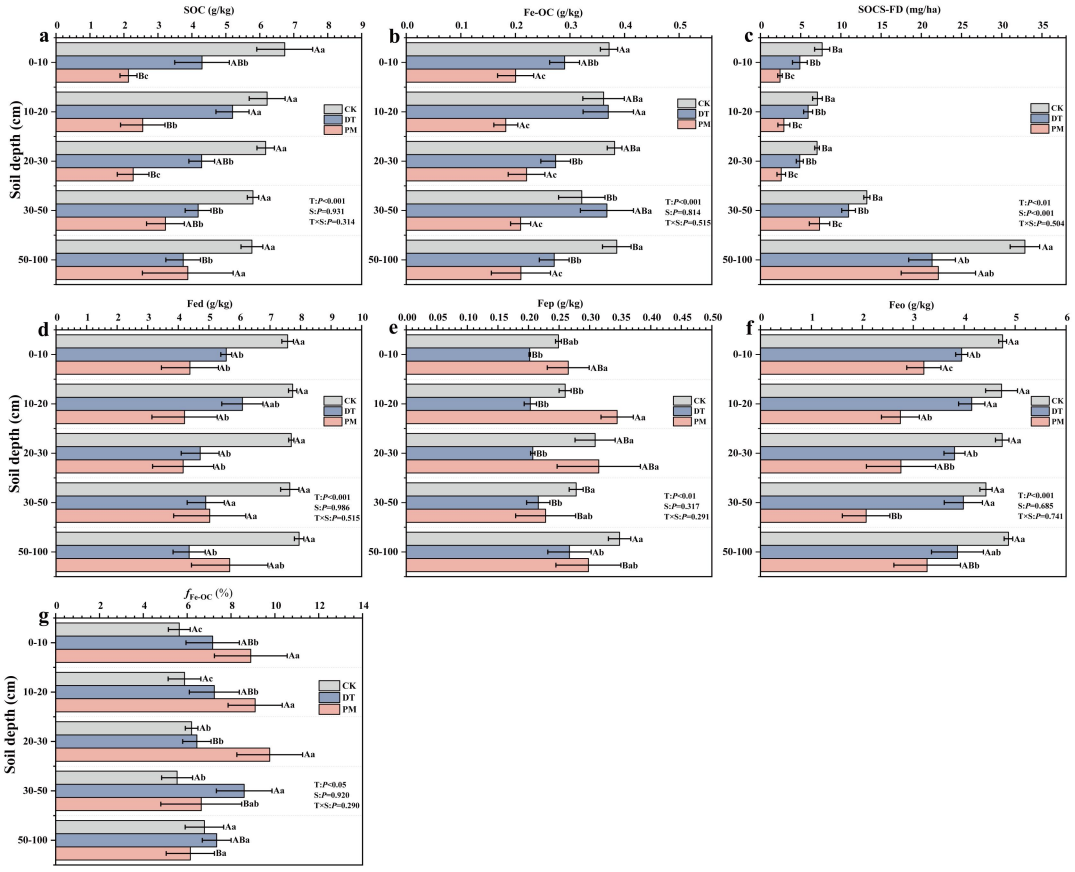

603

604 **Fig. 3** Soil carbon and iron dynamics across soil profiles under different treatments. (a)
605 Total carbon (TC), (b) soil organic carbon (SOC), (c) iron-bound organic carbon
606 (Fe–OC), (d) fixed-depth soil organic carbon stock (SOCS-FD), (e)
607 pyrophosphate-extractable Fe (Fep), (f) dithionite-extractable Fe (Fed), (g)
608 oxalate-extractable Fe (Feo), (h) proportion of iron-bound organic carbon $f_{Fe\text{-}OC}$ (%)
609 across different soil depths under CK (control), DT (deep tillage), and PM (plastic
610 mulching) treatments. Bars represent the mean ± standard error, and lowercase letters
611 above the bars indicate significant differences between treatments at the same soil
612 depth ($P < 0.05$), while uppercase letters indicate significant differences between soil
613 depths within the same treatment ($P < 0.05$).

614

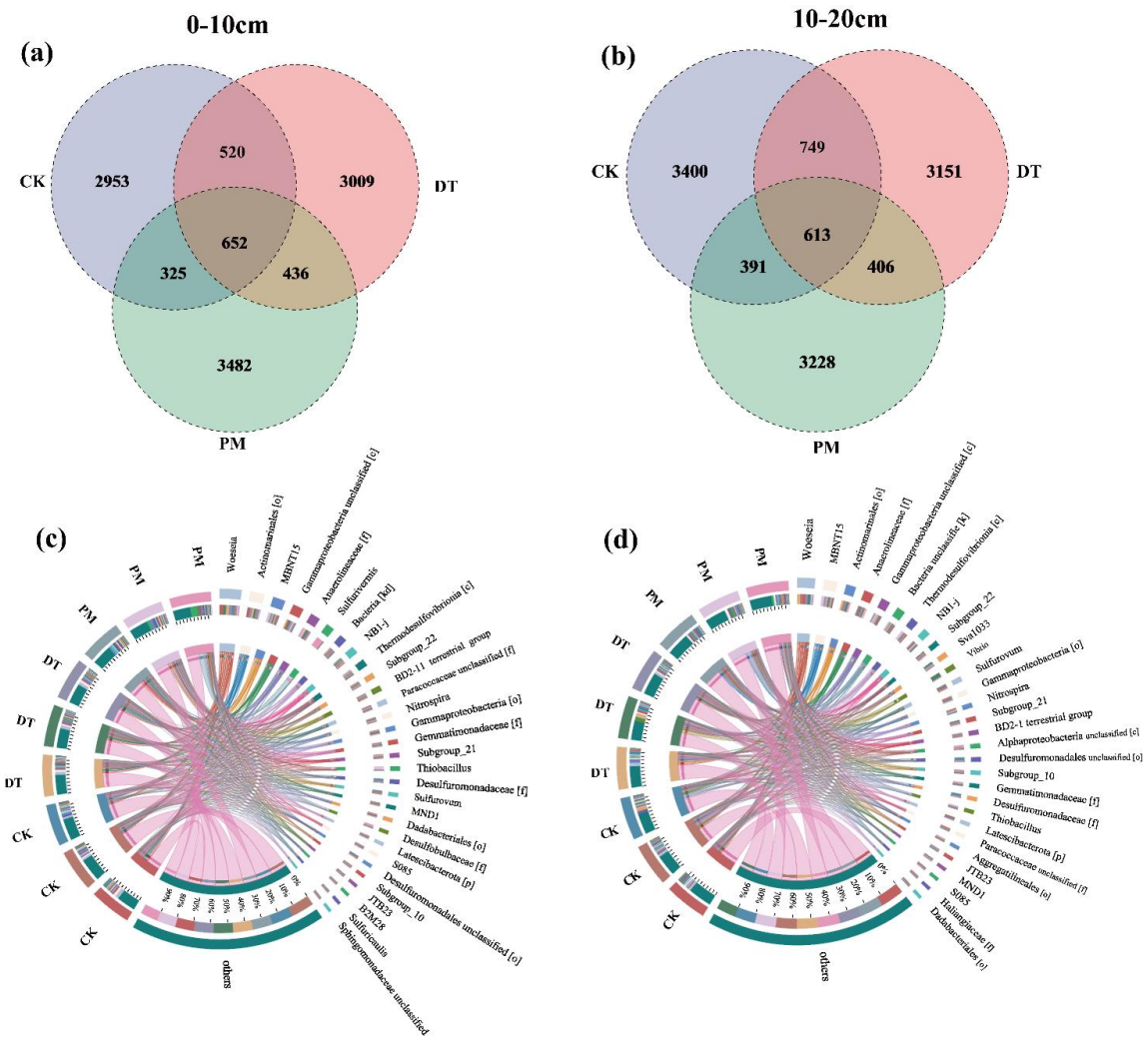

Fig. 4 Taxonomic composition and treatment-specific shifts in soil bacterial communities. (a, b) Venn diagrams showing the numbers of shared and unique amplicon sequence variants (ASVs) among CK (control), DT (deep tillage), and PM (plastic mulching) treatments in the 0–10 cm (a) and 10–20 cm (b) soil layers. (c, d) Circos plots depicting the relative abundance and treatment connectivity of dominant bacterial genera in the 0–10 cm (c) and 10–20 cm (d) soil layers under CK, DT, and PM treatments.

The Circos plots reveal that CK exhibited the highest connectivity among dominant genera in both layers, while PM significantly reduced inter-genus correlations, particularly in the 0 – 10 cm layer. DT induced moderate shifts in genus-level interactions, with Streptomyces and Bacillus showing enhanced co-occurrence under DT versus CK. Relative abundance of Sphingomonas increased markedly under PM in the surface layer, whereas Gemmatimonas declined across all treatments below 10

cm. These patterns suggest that tillage intensity and mulching jointly reshape bacterial network architecture and taxonomic dominance in a depth-dependent manner.

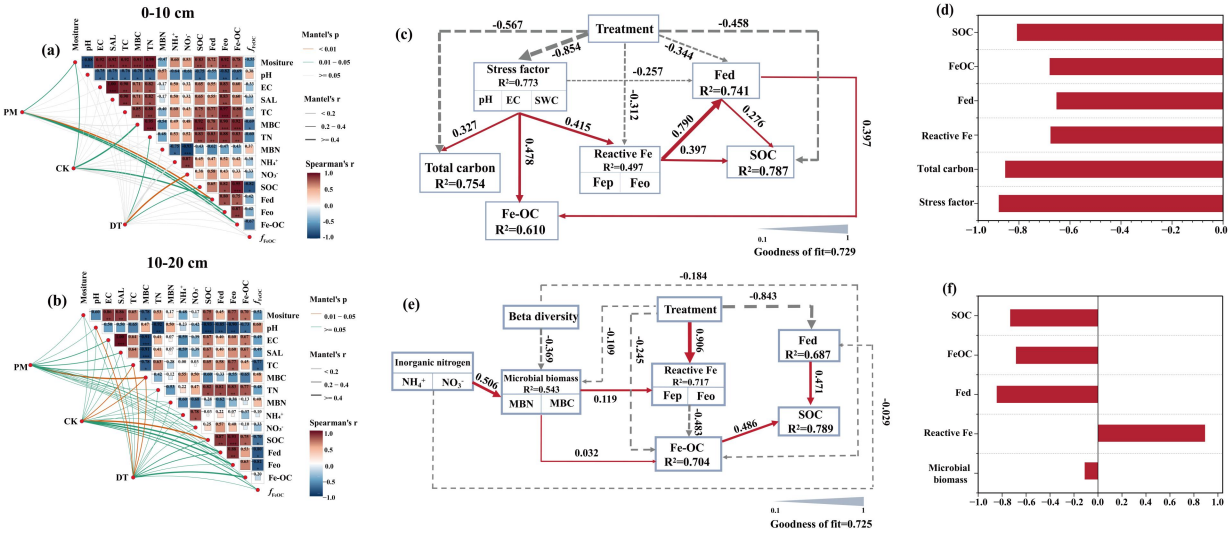

Fig. 5 Mantel tests and partial least squares path models (PLS-PM) linking soil environmental variables, bacterial communities, and soil C fractions under different *S. alterniflora* management states. (a, b) Mantel tests between bacterial community composition and environmental variables at 0–10 cm (a) and 10–20 cm (b). Arrows indicate significant correlations (Mantel's r ≥ 0.4, $P < 0.01$). (c) PLS-PM showing hypothesized associations among management, soil physicochemical variables, reactive Fe pools, and soil C fractions. (d) Standardized total effects of model components on Fe–OC. (e, f) Surface-soil PLS-PM models including bacterial community attributes for 0–20 cm soils. SAL, salinity; EC, electrical conductivity; SOC, soil organic carbon; TC, total carbon; MBC, microbial biomass carbon; TN, total nitrogen; Fe–OC, iron-bound organic carbon; Fep, pyrophosphate-extractable Fe; Feo, oxalate-extractable Fe; Fed, dithionite-extractable Fe.

Acknowledgments

We would like to acknowledge the assistance of Zhu Xiaohong from the Wetland Ecosystem Research Station of Hangzhou Bay for her support in field sampling.

Funding

Funding for this study was provided by the Fundamental Research Funds of CAF (CAFYBB2024MA029), the Open Fund for the Wetland Water Resources Research and Conservation Project from Hangzhou Normal University (HZNU-KFJJ2025), the Pioneer and Leading Goose R&D Program of Zhejiang (2025C02050, 2025C02230, and 2024C02002), the National Key Research and Development Program of China (2023YFE0101700), and the Key R&D Program of Zhejiang (2024C03236).

Conflict of interest

The authors declare that they have no known competing financial interests or personal relationships that could have appeared to influence the work reported in this paper.

Author contributions

Jingwen Gao: Writing-original draft, Visualization, Software, Methodology Investigation, Formal analysis. **Pengcheng Jiang**: Software, Methodology, Investigation **Xiaofei Ye**: Investigation, **Xingna Lin**: Investigation. **Xuexin Shao**: Investigation. **Ming Wu**: Supervision, Investigation and Funding acquisition. **Niu Li:** Writing-review & editing, Validation, Supervision, Software, Resources, Project administration, Investigation, Funding acquisition.

Data availability

Raw data of the study in Wetland Ecosystem Research Station of Hangzhou Bay are available at https://pan.baidu.com/s/1GfHljucHF6jOfE8e4WXz3w

Reference

669 Asanopoulos, C. H., Baldock, J. A., Macdonald, L. M., and Cavagnaro, T. R.:
670 Quantifying blue carbon and nitrogen stocks in surface soils of temperate coastal
671 wetlands, Soil Res., 59, 619–629, https://doi.org/10.1071/SR20040, 2021.
672 Ascenzi, I., Hilbers, J., van Katwijk, M. M., Huijbregts, M. A. J., and Hanssen, S. V.:
673 Increased but not pristine soil organic carbon stocks in restored ecosystems, Nat.
674 Commun., 16, 637, https://doi.org/10.1038/s41467-025-55980-1, 2025.
675 Berg, J. S., Jézéquel, D., Duverger, A., Lamy, D., Laberty-Robert, C., and Miot, J.:
676 Microbial diversity involved in iron and cryptic sulfur cycling in the ferruginous,
677 low-sulfate waters of Lake Pavin, PLoS ONE, 14, e0212787,
678 https://doi.org/10.1371/journal.pone.0212787, 2019.
679 Bhan, M., Misher, C., Hiremath, A., and Vanak, A. T.: Restoration maintains high
680 soil carbon stocks in Asia's largest tropical grassland, Ecol. Appl., 35, e70073,
681 https://doi.org/10.1002/eap.70073, 2025.
682 Brookes, P. C., Landman, A., Pruden, G., and Jenkinson, D. S.: Chloroform
683 fumigation and the release of soil nitrogen: A rapid direct extraction method to
684 measure microbial biomass nitrogen in soil, Soil Biol. Biochem., 17, 837–842,
685 https://doi.org/10.1016/0038-0717(85)90144-0, 1985.
686 Chen, S., Wang, F., Zhang, Y., Qin, S., Wei, S., Wang, S., Hu, C., and Liu, B.:
687 Organic carbon availability limiting microbial denitrification in the deep vadose zone,
688 Environ. Microbiol., 20, 980–992, https://doi.org/10.1111/1462-2920.14027, 2018.
689 Chen, J., Seven, J., Zilla, T., Dippold, M. A., Blagodatskaya, E., and Kuzyakov, Y.:
690 Microbial C:N:P stoichiometry and turnover depend on nutrients availability in soil: a
691 ^{14}C, ^{15}N and ^{33}P triple labelling study, Soil Biol. Biochem., 131, 206–216,
692 https://doi.org/10.1016/j.soilbio.2019.01.017, 2019.
693 Chen, S., Gao, D., Zhang, J., Müller, C., Li, X., Zheng, Y., Dong, H., Yin, G., Han, P.,
694 Liang, X., Liu, M., and Hou, L.: Invasive Spartina alterniflora accelerates soil gross
695 nitrogen transformations to optimize its nitrogen acquisition in an estuarine and
696 coastal wetland of China, Soil Biol. Biochem., 174, 108835,
697 https://doi.org/10.1016/j.soilbio.2022.108835, 2022.
698 Chen, H.-Y., Ge, Z.-M., Zhu, K.-H., Zhao, W., Chen, X.-C., Li, X.-Z., Xin, P., Zhou,

Z., Chen, S., and Bellerby, R.: Ecosystem carbon and nitrogen recovery in restored coastal wetlands, Commun. Earth Environ., 7, 8, https://doi.org/10.1038/s43247-025-03036-z, 2026.

Daugherty, E. E., Gilbert, B., Nico, P. S., and Borch, T.: Complexation and redox buffering of iron (II) by dissolved organic matter, Environ. Sci. Technol., 51, 11096–11104, https://doi.org/10.1021/acs.est.7b03152, 2017.

Feng, X., Zhao, Y., Wang, H., and Liu, C.: Iron–organic carbon interactions in wetlands: Implications for wetland carbon preservation under global changes, Glob. Change Biol., 31, e70300, https://doi.org/10.1111/gcb.70300, 2025.

Garber, A. I., Cohen, A. B., Nealson, K. H., Ramírez, G. A., McAllister, S. M., and Chan, C. S.: Metagenomic insights into the microbial iron cycle of subseafloor habitats, Front. Microbiol., 12, 667944, https://doi.org/10.3389/fmicb.2021.667944, 2021.

Hao, Q., Song, Z., Zhang, X., He, D., Guo, L., van Zwieten, L., Yu, C., Wang, Y., Wang, W., Fang, Y., Fang, Y., Liu, C.-Q., and Wang, H.: Organic blue carbon sequestration in vegetated coastal wetlands: Processes and influencing factors, Earth-Sci. Rev., 255, 104853, https://doi.org/10.1016/j.earscirev.2024.104853, 2024.

Henseler, J., Hubona, G., and Ray, P. A.: Using PLS path modeling in new technology research: updated guidelines, Ind. Manage. Data Syst., 116, 2–20, https://doi.org/10.1108/IMDS-09-2015-0382, 2016.

Hernandez, D. J., David, A. S., Menges, E. S., Searcy, C. A., and Afkhami, M. E.: Environmental stress destabilizes microbial networks, ISME J., 15, 1722–1734, https://doi.org/10.1038/s41396-020-00882-x, 2021.

Huang, L., Zhang, G., Bai, J., Xia, Z., Wang, W., Jia, J., Wang, X., Liu, X., and Cui, B.: Desalinization via freshwater restoration highly improved microbial diversity, co-occurrence patterns and functions in coastal wetland soils, Sci. Total Environ., 765, 142769, https://doi.org/10.1016/j.scitotenv.2020.142769, 2021.

Jia, Z., Huang, X., Li, L., Li, T., Duan, Y., Ling, N., and Yu, G.: Rejuvenation of iron oxides enhances carbon sequestration by the “iron gate” and “enzyme latch” mechanisms in a rice–wheat cropping system, Sci. Total Environ., 839, 156209,

https://doi.org/10.1016/j.scitotenv.2022.156209, 2022.

Joergensen, R. G. and Mueller, T.: The fumigation-extraction method to estimate soil microbial biomass: Calibration of the kEN value, Soil Biol. Biochem., 28, 33–37, 1996.

Li, H., Mao, D., Wang, Z., Huang, X., Li, L., and Jia, M.: Invasion of Spartina alterniflora in the coastal zone of mainland China: Control achievements from 2015 to 2020 towards the Sustainable Development Goals, J. Environ. Manage., 323, 116242, https://doi.org/10.1016/j.jenvman.2022.116242, 2022.

Li, T., Zeng, J., He, B., and Chen, Z.: Changes in soil C, N, and P concentrations and stoichiometry in karst trough valley area under ecological restoration: The role of slope aspect, land use, and soil depth, Forests, 12, 144, https://doi.org/10.3390/f12020144, 2021.

Libbey, K. and Hernández, D. L.: Depth profile of soil carbon and nitrogen accumulation over two decades in a prairie restoration experiment, Ecosystems, 24, 1348–1360, https://doi.org/10.1007/s10021-020-00588-3, 2021.

Lin, G. and Lin, X.: Bait input altered microbial community structure and increased greenhouse gases production in coastal wetland sediment, Water Res., 218, 118520, https://doi.org/10.1016/j.watres.2022.118520, 2022.

Lin, X., Zhu, B., Peng, Y., Lin, G., Sun, D., and Ye, W.: Responses of microbial communities and greenhouse gas production to land use change in mangrove wetland sediments, Limnol. Oceanogr., 70, 1210–1225, https://doi.org/10.1002/lno.70028, 2025.

Liu, Z., Song, Y., Qin, X., Yuan, J., Lou, Y., Yang, C., Tang, H., and Song, C.: Deep soil microbial carbon metabolic function is important but often neglected: A study on the Songnen Plain reed wetland, Northeast China, Fundam. Res., 3, 833–843, https://doi.org/10.1016/j.fmre.2022.06.013, 2022.

Lovley, D. R. and Phillips, E. J. P.: Novel mode of microbial energy metabolism: Organic carbon oxidation coupled to dissimilatory reduction of iron or manganese, Appl. Environ. Microbiol., 54, 1472–1480, https://doi.org/10.1128/aem.54.6.1472-1480.1988, 1988.

759 Luo, S., Yuan, J., Song, Y., Ren, J., Qi, J., Zhu, M., Feng, Y., Li, M., Wang, B., Li, X.,
760 and Song, C.: Elevated salinity decreases microbial community complexity and
761 carbon, nitrogen and phosphorus metabolism in the Songnen Plain wetlands of China,
762 Water Res., 276, 123285, https://doi.org/10.1016/j.watres.2025.123285, 2025.
763 Mack, S. K., Lane, R. R., Deng, J., Morris, J. T., and Bauer, J. J.: Wetland carbon
764 models: applications for wetland carbon commercialization, Ecol. Model., 476,
765 110228, https://doi.org/10.1016/j.ecolmodel.2022.110228, 2023.
766 Murdiyarso, D., Krisnawati, H., Adinugroho, W. C., and Sasmito, S. D.: Deriving
767 emission factors for mangrove blue carbon ecosystem in Indonesia, Carbon Balance
768 Manage., 18, 22, https://doi.org/10.1186/s13021-023-00233-1, 2023.
769 Ni, B., Yu, X., Duan, X., and Zou, Y.: Wetland soil organic carbon balance is
770 reversed by old carbon and iron oxide additions, Front. Microbiol., 14, 1327265,
771 https://doi.org/10.3389/fmicb.2023.1327265, 2024.
772 Oren, A., Rotbart, N., Borisover, M., and Bar-Tal, A.: Chloroform fumigation
773 extraction for measuring soil microbial biomass: The validity of using samples
774 approaching water saturation, Geoderma, 318, 138–145,
775 https://doi.org/10.1016/j.geoderma.2018.01.007, 2018.
776 Peng, Y. J., Chahal, I., Hooker, D. C., and Van Eerd, L. L.: Comparison of equivalent
777 soil mass approaches to estimate soil organic stocks under long-term tillage, Soil
778 Tillage Res., 238, 106021, https://doi.org/10.1016/j.still.2024.106021, 2024.
779 Poulton, S. W. and Canfield, D. E.: Development of a sequential extraction procedure
780 for iron: Implications for iron partitioning in continentally derived particulates, Chem.
781 Geol., 214, 209–221, https://doi.org/10.1016/j.chemgeo.2004.09.003, 2005.
782 Rogers, K., Kelleway, J., Saintilan, N., Megonigal, J., Adams, J., Holmquist, J., Lu,
783 M., Lu, M., Schile-Beers, L., Zawadzki, A., Mazumder, D., and Woodroffe, C.:
784 Wetland carbon storage controlled by millennial-scale variation in relative sea-level
785 rise, Nature, 567, 91–95, https://doi.org/10.1038/s41586-019-0951-7, 2019.
786 Rowland, P. I., Wartman, M., Bursic, J., and Carnell, P.: Restored and created tidal
787 marshes recover ecosystem services over time, Environ. Sustain. Indic., 24, 100539,
788 https://doi.org/10.1016/j.indic.2024.100539, 2024.

789 Sadat-Noori, M., Andersen, M. S., Waddington, K., Ruprecht, J., Tucker, T. A., and
790 Glamore, W.: Groundwater driven carbon fluxes in a restored coastal saltmarsh
791 wetland: implications for coastal wetland restoration, J. Hydrol., 643, 131997,
792 https://doi.org/10.1016/j.jhydrol.2024.131997, 2024.

793 Wagai, R. and Mayer, K. U.: Iron-bound organic carbon in forest soils: quantification
794 and characterization, Soil Biol. Biochem., 39, 2438–2452,
795 https://doi.org/10.1016/j.soilbio.2007.04.004, 2007.

796 Wang, Y., Wang, H., He, J.-S., and Feng, X.: Iron-mediated soil carbon response to
797 water-table decline in an alpine wetland, Nat. Commun., 8, 15972,
798 https://doi.org/10.1038/ncomms15972, 2017.

799 Wang, Y., Liu, X., Zhang, X., Dai, G., Wang, Z., and Feng, X.: Evaluating wetland
800 soil carbon stability related to iron transformation during redox oscillations,
801 Geoderma, 428, 116222, https://doi.org/10.1016/j.geoderma.2022.116222, 2022.

802 Wang, Q., Cui, G., Liu, H., Huang, X., Xiao, X., Wang, M., Jia, M., Mao, D., Li, X.,
803 Xiao, Y., and Li, H.: Spatiotemporal dynamics and potential distribution prediction of
804 Spartina alterniflora invasion in Bohai Bay based on Sentinel time-series data and
805 MaxEnt modeling, Remote Sens., 17, 975, https://doi.org/10.3390/rs17060975,
806 2025a.

807 Wang, X., Xia, X., Riaz, M., Babar, S., El-Desouki, Z., Qasim, M., Wang, J., and
808 Jiang, C.: Biochar amendment modulate microbial community assembly to mitigate
809 saline-alkaline stress across soil depths, J. Environ. Manage., 385, 125574,
810 https://doi.org/10.1016/j.jenvman.2025.125574, 2025b.

811 Wang, X., Zhang, J., Yang, B., Mao, H., Yu, Q., and Zhang, Y.: Intermittent
812 microaeration enhanced anaerobic digestion: the key role of Fe(III)/Fe(II) cycle and
813 reactive oxygen species, Environ. Sci. Technol., 59, 8629–8639,
814 https://doi.org/10.1021/acs.est.5c04187, 2025c.

815 Wen, S., Chen, J., Yang, Z., Deng, L., Feng, J., Zhang, W., Zeng, X., Huang, Q.,
816 Delgado-Baquerizo, M., and Liu, Y.-R.: Climatic seasonality challenges the stability
817 of microbial-driven deep soil carbon accumulation across China, Glob. Change Biol.,

29, 4430–4439, https://doi.org/10.1111/gcb.16760, 2023.

Wendt, J. W. and Hauser, S.: An equivalent soil mass procedure for monitoring soil organic carbon in multiple soil layers, Eur. J. Soil Sci., 64, 58–65, https://doi.org/10.1111/ejss.12002, 2013.

Wu, B., Tang, X., Song, Z., Qi, M., Liu, M., Li, X., and Hou, L.: Chemoautotrophic carbon fixation favors iron-bound organic carbon formation in estuarine and coastal sediments, Environ. Sci. Technol., 59, 12642–12655, https://doi.org/10.1021/acs.est.5c00324, 2025a.

Wu, L., Song, Z., Xiao, Z., Zhang, X., Van Zwieten, L., Guo, L., Li, Z., Yang, X., Zhao, X., Wang, Y., He, D., Wang, W., Liu, C., and Wang, H.: Assessment of soil organic and inorganic carbon stocks in coastal salt marshes of China: key mechanisms elucidated, Glob. Change Biol., 31, e70421, https://doi.org/10.1111/gcb.70421, 2025b.

Xia, S., Song, Z., Li, Q., Guo, L., Yu, C., Singh, B. P., Fu, X., Chen, C., Wang, Y., and Wang, H.: Distribution, sources, and decomposition of soil organic matter along a salinity gradient in estuarine wetlands characterized by C:N ratio, $\delta^{13}C$–$\delta^{15}N$ and lignin biomarker, Glob. Change Biol., 27, 417–434, https://doi.org/10.1111/gcb.15403, 2021.

Xia, S., Song, Z., Van Zwieten, L., Guo, L., Yu, C., Wang, W., Li, Q., Hartley, I., Yang, Y., Liu, H., Wang, Y., Ran, X., Liu, C., and Wang, H.: Storage, patterns and influencing factors for soil organic carbon in coastal wetlands of China, Glob. Change Biol., 28, 6065–6085, https://doi.org/10.1111/gcb.16325, 2022.

Xiao, L., Zhang, W., Hu, P., Xiao, D., Yang, R., Ye, Y., and Wang, K.: The formation of large macroaggregates induces soil organic carbon sequestration in short-term cropland restoration in a typical karst area, Sci. Total Environ., 801, 149588, https://doi.org/10.1016/j.scitotenv.2021.149588, 2021.

Yang, R., Yang, S., Chen, L., Yang, Z., Xu, L., Zhang, X., Liu, G., Jiao, C., Bai, R., Zhang, X., Zhai, B., Wang, Z., Zheng, W., Li, Z., and Zamanian, K.: Effect of vegetation restoration on soil erosion control and soil carbon and nitrogen dynamics: A meta-analysis, Soil Tillage Res., 230, 105705,

https://doi.org/10.1016/j.still.2023.105705, 2023.

Yang, Y., Zhao, Z., and Zhang, Y.: Anaerobic ammonium removal pathway driven by the Fe(II)/Fe(III) cycle through intermittent aeration, Environ. Sci. Technol., 55, 7615–7623, https://doi.org/10.1021/acs.est.0c08624, 2021.

Yu, C., Xie, S., Song, Z., Xia, S., and Aström, M. E.: Biogeochemical cycling of iron (hydr-)oxides and its impact on organic carbon turnover in coastal wetlands: A global synthesis and perspective, Earth-Sci. Rev., 218, 103658, https://doi.org/10.1016/j.earscirev.2021.103658, 2021.

Zhang, B., Xu, C., Zhang, Z., Hu, C., He, Y., Huang, K., Pang, Q., and Hu, G.: Response of soil organic carbon and its fractions to natural vegetation restoration in a tropical karst area, southwest China, Front. For. Glob. Change, 6, 1172062, https://doi.org/10.3389/ffgc.2023.1172062, 2023.

Zhang, D., Cai, X., Diao, L., Wang, Y., Wang, J., An, S., Cheng, X., and Yang, W.: Changes in soil organic carbon and nitrogen pool sizes, dynamics, and biochemical stability during ~160 years natural vegetation restoration on the Loess Plateau, China, Catena, 211, 106014, https://doi.org/10.1016/j.catena.2021.106014, 2022.

Zhang, G., Bai, J., Tebbe, C. C., Zhao, Q., Jia, J., Wang, W., Wang, X., and Yu, L.: Salinity controls soil microbial community structure and function in coastal estuarine wetlands, Environ. Microbiol., 23, 1020–1037, https://doi.org/10.1111/1462-2920.15281, 2021.

Zhang, J., Zhao, S., Miao, Q., Feng, L., Chi, Z., Li, Z., Shuai, K., Chen, X., Liu, Y., Hu, R., Peng, G., Li, J., Hu, Y., Su, Z., Fang, M., and Li, J.: Effect of subsurface drainage in regulating water on desalinization and microbial communities in salinized irrigation soils, Agronomy, 14, 282, https://doi.org/10.3390/agronomy14020282, 2024.

Zhao, N., Ding, H., Zhou, X., Guillemot, T., Zhang, Z., Zhou, N., and Wang, H.: Dissimilatory iron-reducing microorganisms: The phylogeny, physiology, applications and outlook, Crit. Rev. Environ. Sci. Technol., 55, 73–98, https://doi.org/10.1080/10643389.2024.2382498, 2025.

Zheng, B., Xiao, Z., Liu, J., Zhu, Y., Shuai, K., Chen, X., Liu, Y., Hu, R., Peng, G., Li,

J., Hu, Y., Su, Z., Fang, M., and Li, J.: Vertical differences in carbon metabolic diversity and dominant flora of soil bacterial communities in farmlands, Sci. Rep., 14, 60142, https://doi.org/10.1038/s41598-024-60142-2, 2024.

Zheng, J., Sun, L., Zhong, L., Yuan, Y., Wang, X., Wu, Y., Lu, C., Xue, S., and Song, Y.: Allometric growth and carbon sequestration of young Kandelia obovata plantations in a constructed urban coastal wetland in Haicang Bay, Southeast China, Forests, 16, 1126, https://doi.org/10.3390/f16071126, 2025.

Zhu, Z., Zhou, J., Shahbaz, M., Tang, H., Liu, S., Zhang, W., Yuan, H., Zhou, P., Alharbi, H., Wu, J., Kuzyakov, Y., and Ge, T.: Microorganisms maintain C:N stoichiometric balance by regulating the priming effect in long-term fertilized soils, Appl. Soil Ecol., 167, 104033, https://doi.org/10.1016/j.apsoil.2021.104033, 2021.